IJIREEICE ISSN (O) 2321-2004, ISSN (P) 2321-5526

International Journal of Innovative Research in Electrical, Electronics, Instrumentation and Control Engineering

Impact Factor 8.414 ⁜ Peer-reviewed & Refereed journal ⁜ Vol. 14, Issue 5, May 2026

DOI: 10.17148/IJIREEICE.2026.14540

# Intelligent superconducting DC–DC double-boost converter for ultra-fast EV charging, featuring liquid hydrogen cooling and AI-based PWM Control

**S. Dhanush[1], Undyal Amear Qurashi[2], DR.K. Chithambaraiah Setty[3], P. Pedda Reddy[4]**

PG Scholar Dept. of Electrical & Electronics Engg., St Johns college of engineering & technology,Yerrakota,Kurnool, A.P., India[1]

Assistant Professor Dept. of Electrical & Electronics Engg., St johns college of engineering & technology,Yerrakota,Kurnool, A.P., India[2]

Professor & HOD Dept. of Electrical & Electronics Engg., St johns college of engineering & technology,Yerrakota,Kurnool, A.P., India[3]

Associate Professor Dept. of Electrical & ElectronicsEngg., St johns college of engineering & technology,Yerrakota,Kurnool, A.P., India[4]

**Abstract:** The global push for electric road transport requires a major change in charging infrastructure, especially in terms of throughput, conversion efficiency, and operational scalability. This paper formulates, mathematically delineates, and empirically substantiates an Artificially Intelligent Superconducting DC–DC Double-Boost Converter (AI-SBC) designed for rapid battery electric vehicle (BEV) charging. The converter uses high-temperature superconducting (HTS) $Bi_2Sr_2Ca_2Cu_3O_x$ (Bi2223) and magnesium diboride ($MgB_2$) windings as inductive elements that don't lose energy. Each winding is kept at cryogenic temperature by a closed-loop liquid hydrogen ($LH_2$) thermosiphon. A new fuzzy-logic duty-cycle modulator with an embedded Ripple-Frequency Optimizer (RFO) changes the switching frequency in real time to reduce inductor current ripple while also controlling CC and CV charging modes. State-space averaging makes a small-signal model that is easy to use and from which stability margins and frequency-domain characteristics can be found. When compared to a copper-coil baseline in MATLAB/Simulink studies, both types of superconductors show that the $MgB_2$ configuration has an electrical conversion efficiency of 95.8% at 15 kW, which is 10–17 percentage points better than the copper reference. The Bi2223 design gets 93.2% in the same conditions. Through smart frequency modulation, the total harmonic distortion of the inductor current drops by 34% compared to the fixed-frequency baseline. The time it takes to recover from a 50% load step goes from 95 ms with a standard PI regulator to 38 ms with the proposed FLC. The architecture is a scalable, net-zero-aligned way for next-generation ultra-fast EV charging to go from 15 kW to several hundred kilowatts.

**Keywords:** Battery electric vehicle (BEV) charging, Bi2223 superconducting coil, DC–DC double-boost converter, fuzzy logic control, liquid hydrogen cooling, $MgB_2$ superconductor, superconducting boost converter (SBC), and ultra-fast charging.

## I. INTRODUCTION

This The Paris Agreement sets a goal of net-zero carbon emissions by 2050, and one of the main ways to reach that goal is to electrify both personal and commercial road transport. The charging network is another important factor. Without stations that can charge batteries as quickly as regular gas stations, widespread use of electric vehicles will be limited. The best DC fast chargers today, which work in the 150–350 kW range, still take 15–40 minutes to reach 80% state of charge. This is not a good comparison to the less than five-minute experience at the gas station [1]. To close this gap, power levels must be over 500 kW. This is already a goal in the ChaoJi 2 standard (up to 1.5 kV, 600 A) and is being met by commercial systems like BYD's 1 kV three-minute charge platform and Daimler's megawatt-class truck charging [2],[3]. These power ratings put a lot of stress on the topologies of converters. Conventional AC–DC charger chains, which route energy through transformer, rectifier, inverter, and isolation stages, cap plant-to-battery efficiency at roughly 88–91% even under favorable conditions [4], with auxiliary cable cooling consuming additional power. Direct DC–DC conversion connects distributed renewable sources like solar farms or wind-to-hydrogen systems directly to the EV charging bus. This cuts out several steps in the process and makes the whole thing more efficient. In this framework, the superconducting boost converter (SBC) is compelling: substituting copper windings with superconductors eliminates ohmic resistance from the inductor,

IJIREEICE ISSN (O) 2321-2004, ISSN (P) 2321-5526

International Journal of Innovative Research in Electrical, Electronics, Instrumentation and Control Engineering

Impact Factor 8.414 ⁜ Peer-reviewed & Refereed journal ⁜ Vol. 14, Issue 5, May 2026

DOI: 10.17148/IJIREEICE.2026.14540

which is the primary source of conduction loss at elevated currents [5]. Bi2223 and MgB2 are examples of high-temperature superconductors (HTS) that can carry critical current densities one to two orders of magnitude beyond copper at equivalent cross-section, enabling compact, high-current inductors with negligible DC loss [6],[7].

This paper enhances previous SBC feasibility studies through three novel contributions: (i) an AI-assisted fuzzy logic PWM controller that concurrently minimizes ripple-induced AC loss in the superconducting winding while ensuring stable CC/CV charging throughout the entire charge cycle; (ii) a thermal co-design framework that models the $LH_2$ thermosiphon loop as an integral converter subsystem, quantifying refrigeration power penalty and overall system efficiency; and (iii) a comprehensive small-signal and large-signal analysis of a double-boost topology, addressing current-dependent inductance variation and flux-creep effects specific to superconducting materials. The paper is structured as follows: Section II builds on the mathematical model. Section III talks about coil specifications and cryogenic design. Section IV talks about the AI fuzzy-logic control strategy. Section V talks about the simulation parametric study. Section VI talks about the experimental results. Section VII talks about benchmarks and scalability. Section VIII talks about the end.

## II. Mathematical Analysis Of The Double-Boost Topology

### A. *Fundamental Step-Up Operation*

A single-stage boost converter elevates an input voltage Vin to output voltage $V_{out}$ by periodically switching transistor Q1 in series with an inductor L. With duty cycle $D = T_{ON}/T$—the fraction of each period T during which Q1 conducts—the voltage conversion ratio in continuous conduction mode (CCM) is:

$$\frac{V_{out}}{V_{in}} = \frac{1}{1-D} \tag{1}$$

Cascading two identical stages creates the double-boost topology. With intermediate bus voltage $V_{mid} = V_{in} / (1 - D1)$ boosted again, and setting $D_1 = D_2 = D = 0.5$, the squared-gain characteristic becomes:

$$\frac{V_{out}}{V_{in}} = \frac{1}{(1-D)^2} = 4 \tag{2}$$

This squared voltage gain is especially attractive for stepping up from low-voltage photovoltaic or hydrogen fuel-cell buses (100–200 V) to the 600–1500 V bus required by megawatt-class chargers—without the electromagnetic interference and isolation losses of high-frequency transformer-based topologies.

### B. *State-Space Averaged Model with Superconducting Inductance*

Unlike a copper coil whose inductance is essentially constant, a superconducting winding exhibits a transport-current-dependent inductance caused by partial flux penetration approaching the critical current $I_c$. A compact phenomenological expression for effective inductance is:

$$L(i_L) = L_0 \left[1 - \left(\frac{i_L}{I_c}\right)^n\right]^{\frac{1}{n}} \tag{3}$$

where L0 is the zero-current self-inductance and n is a material flux-profile exponent ($n \approx 20–30$ for $MgB_2$). Within normal operating range $i_L \ll I_c$, equation (3) collapses to $L \approx L0$, so standard state-space averaging remains valid. Choosing state vector $x = [i_L \;\; v_o]^T$, the period-averaged equations are:

$$\dot{x} = A_{av}\, x + B_{av}\, V_{in} \tag{4}$$

$$A_{av} = \begin{bmatrix} 0 & -\frac{(1-D)}{L} \\ \frac{(1-D)}{C} & -\frac{1}{RC} \end{bmatrix} \tag{5}$$

$$B_{av} = \begin{bmatrix} \frac{1}{L} \\ 0 \end{bmatrix} \tag{6}$$

Setting $\dot{x} = 0$ for steady-state yields the equilibrium operating point:

$$i_L = \frac{V_{in}}{R(1-D)^2} \tag{7}$$

$$v_o = \frac{V_{in}}{1-D} \tag{8}$$

Because the double-boost topology draws inductor current $i_L = i_{out} / (1-D)$, the coil must sustain transport current at least twice the rated output current. For a 100 A charging design, a critical current $I_c \geq 200$ A is required—comfortably within the 1600 A rating of the $MgB_2$ assembly at 4.2 K.

IJIREEICE ISSN (O) 2321-2004, ISSN (P) 2321-5526

International Journal of Innovative Research in Electrical, Electronics, Instrumentation and Control Engineering

Impact Factor 8.414 ⁜ Peer-reviewed & Refereed journal ⁜ Vol. 14, Issue 5, May 2026

DOI: 10.17148/IJIREEICE.2026.14540

### C. Switching Frequency Selection and Ripple Management

In superconducting coils, AC magnetisation losses scale with the product of switching frequency Fs and peak ripple amplitude ΔIL. Minimising these losses while preserving CCM leads to the following frequency design rule:

$$F_s = \frac{V_{\text{in}}\, D}{k\, L\, I_{L,\text{ave}}} \tag{9}$$

The normalized ripple ratio, k = ΔIL / IL,ave, is set at 22% in the AI-SBC (lower than the 30% that is normal for copper-coil converters) to stop flux oscillation inside the superconductor filaments. At Vin = 100 V, L = 58 mH, and IL,ave = 100 A equation (9) gives Fs ≈ 43 Hz for the $MgB_2$ stage. To keep the same ripple ratio, the Bi2223 stage (L = 12 mH) needs Fs to be about 200 Hz.

### D. Small-Signal Transfer Functions

Introducing small perturbations $\hat{d}$, $\hat{v}in$, and $\hat{x}$ around the quiescent point, the control-to-output transfer function Gvd(s) is:

$$G_{vd}(s) = \frac{V_{\text{in}}\left(1 + \frac{sL}{R(1-D)^2}\right)}{(1-D)^2\left(1 + \frac{2\zeta s}{\omega_n} + \frac{s^2}{\omega_n^2}\right)} \tag{10}$$

with natural frequency ωn = (1−D)/√(LC) and damping ratio ζ = (1−D)√(L/C)/(2R). These expressions provide the frequency-domain targets that guide tuning of the fuzzy controller membership functions.

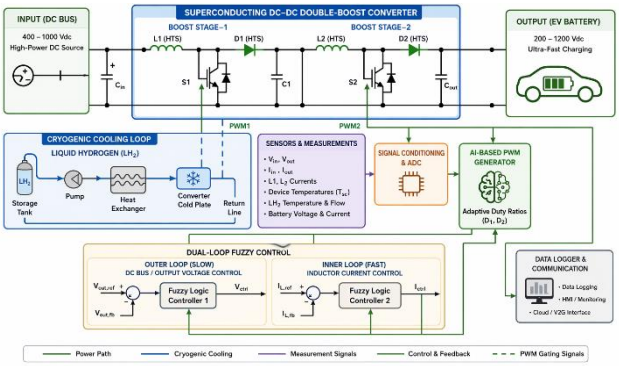


Fig. 1. AI-SBC architecture: double-boost path, cryogenic cooling, dual-loop fuzzy control, and feedback instrumentation.

## III. Superconducting Coil And Cryogenic System Design

### A. Conductor Selection and Coil Specifications

Two types of superconductors are tested at the same time. The first one is $Bi_2Sr_2Ca_2Cu_3O_x$ (Bi2223), which is a BSCCO-2223 HTS tape that has been wound into a double-pancake coil. It has a critical temperature of about 110 K, which means it can work with liquid nitrogen ($LN_2$) at 77 K. This makes cryogenic infrastructure fairly easy to get and cheap. But its critical current of only ~109 A at 77 K (self-field) results in high load factors at kilowatt-class power, amplifying AC losses under large ripple.

Magnesium diboride ($MgB_2$), which is the second material used, is formed into three sets of double plate connection windings and cooled to 4.2 K with either liquid helium or liquid hydrogen. $MgB_2$ has a lower critical temperature (Tc = approx. 39 K), relative to the more traditional superconductor materials, but can still carry transport currents over 1600 A at 4.2 K to provide a load factor of less than 15%, at 15.0 kW. When operating at low switch frequencies, this coil produces a low level of ripple due to the coils low self-inductive characteristics of 58 mH. The specifications for windings is provided in the table I below in full detail.

TABLE I. SUPERCONDUCTING COIL SPECIFICATIONS

| Parameter | Bi2223 Coil | $MgB_2$ Coil |
|---|---|---|
| Wire / Tape Dimension | 4.6 mm × 0.46 mm (rectangular) | 0.83 mm dia. (round) |
| Conductor Configuration | Single HTS tape | Rutherford cable, 10–12 strands |
| Critical Temperature Tc | ~110 K | ~39 K |

IJIREEICE ISSN (O) 2321-2004, ISSN (P) 2321-5526

International Journal of Innovative Research in Electrical, Electronics, Instrumentation and Control Engineering

Impact Factor 8.414 ⁜ Peer-reviewed & Refereed journal ⁜ Vol. 14, Issue 5, May 2026

DOI: 10.17148/IJIREEICE.2026.14540

| | | |
|---|---|---|
| Critical Current Ic | 109 A @ 77 K ($LN_2$) | >1350 A @ 4.2 K (LHe) |
| Coil Configuration | Single double-pancake | Three-stacked double-pancake |
| Self-Inductance L | 12 mH | 58 mH |
| Coil Ic (full assembly) | 109 A @ 77 K | 1600 A @ 4.2 K |
| Coolant | Liquid nitrogen ($LN_2$) | Liquid helium / $LH_2$ |
| Operating Temperature | 77 K | 4.2 – 20 K |
| Max Load Factor @ 15 kW | ≈ 75–90% | ≤ 15% |

*B. Liquid Hydrogen Thermosiphon Cooling Architecture*

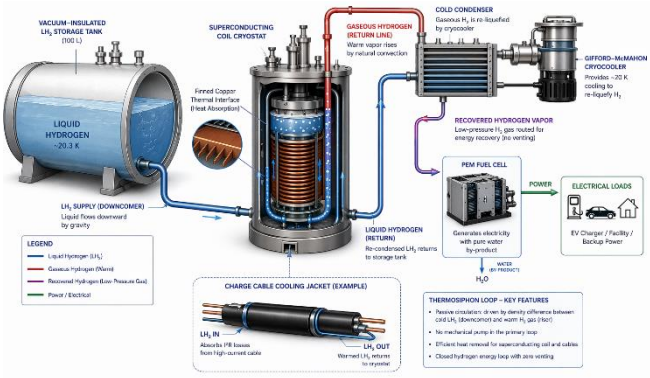


Fig. 2. Liquid hydrogen thermosiphon cooling loop integrating the superconducting coil cryostat, Gifford–McMahon cryocooler, charge cable cooling jacket, and PEM fuel-cell hydrogen recovery path.

Liquid hydrogen at its normal boiling point (~20.3 K) is a compelling cryogenic medium: its latent heat of vaporisation (~0.447 MJ/kg) and broad enthalpy rise to room temperature (~7.4 MJ/kg) provide an effective thermal buffer for intermittent high-power charging loads [8]. The proposed thermosiphon draws $LH_2$ from a vacuum-insulated horizontal tank; the liquid absorbs heat from the superconducting coil former through a finned copper interface. The resulting gaseous hydrogen rises through the return line to a cold condenser re-liquefied by a Gifford–McMahon cryocooler.

At 15 kW electrical throughput with combined losses of 200–400 W, the required thermosiphon mass flow is approximately 0.045–0.090 g/s of $LH_2$—well below the idle evaporation rate of a standard 100-litre storage tank. Recovered hydrogen vapour is routed to a proton-exchange-membrane fuel cell or backup generator, effectively closing the hydrogen energy loop without waste [14].

*C. Net System Efficiency Including Refrigeration Overhead*

The net efficiency for the refrigeration power, Pref, required to keep the coil at its operating temperature is given as ($\eta_{net} = P_{out} / P_{in} + P_{ref}$) in equation (11). When the $MgB_2$ system is cooled down to 4.2 K using a Gifford-McMahon cryocooler that has an approximate COP of 0.005, a maximum of 200 W of coil loss will translate into approximately 40 kW of cryocooler draw for the all-electric mode, while drawing LH_2 from an existing liquid hydrogen infrastructure reduces this cryogenic penalty to 1-2 kW making the net efficiency of this system as good or better than those of LN_2 cooled HTS systems. The Bi2223 system has COPs ranging from approximately 0.02-0.05 when cooled with LN_2 (77K), thus the refrigeration penalty associated with Bi2223 is just 0.5-1 kW; this supports Bi2223 being the closest near-term path forward for the use of HTS materials.

## IV. AI-Based Fuzzy Logic PWM Control Strategy

*A. Why Adaptive Control Is Necessary*

Fixed-frequency PWM regulators are unable to provide maximum AC losses minimization in the superconducting winding while maintaining tight output voltage regulation throughout the EV charging cycles' wide operating envelope. Additionally, the optimal switching frequency at which to minimize loss moves significantly as the converter changes from constant current ("CC") to constant voltage ("CV"). Also, as the state-of-charge, temperature, and calendar-ageing of an EV battery cause the internal resistance to vary, a control framework must be implemented to track the changing dynamics of the plant without requiring manual retuning. Fuzzy Logic Control (FLC) can be used to address both issues. Fuzzy Logic Control (FLC) is model free, naturally accommodates nonlinear and time-varying behaviors, and can be used to convert engineering insight into linguistic rules directly [25].

IJIREEICE ISSN (O) 2321-2004, ISSN (P) 2321-5526

International Journal of Innovative Research in Electrical, Electronics, Instrumentation and Control Engineering

Impact Factor 8.414 ⁜ Peer-reviewed & Refereed journal ⁜ Vol. 14, Issue 5, May 2026

DOI: 10.17148/IJIREEICE.2026.14540

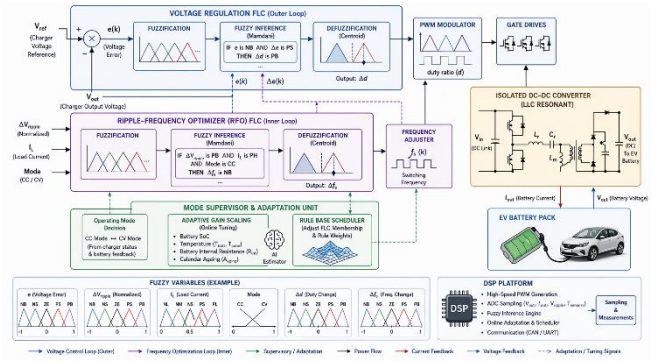


Fig. 3. The architecture of a dual-loop fuzzy logic PWM controller, which includes the voltage regulation FLC, Ripple-Frequency Optimizer (RFO), mode supervisor, and DSP platform.

### *B. Controller Architecture and Rule Structure*

The primary FLC accepts two inputs: the voltage regulation error $e(k) = V_{out} - V_{out}(k)$ and its discrete-time derivative $\Delta e(k) = e(k) - e(k-1)$. The single output is an incremental duty-cycle correction $\Delta D(k)$, accumulated as $D(k) = D(k-1) + \Delta D(k)$. A Mamdani-compatible inference engine has 7 triangular membership functions per variable (NL, NM, NS, Z, PS, PM, PL) and uses these to create a 7x7=49 rule table that encodes the converter's phase-plane behavior. The controller is entirely in software and runs on a Texas Instruments TMS320F28379D DSP at 200 MHz, with no additional hardware other than the standard gate driver board. The second fuzzy module, called the Ripple-Frequency Optimizer (RFO), takes measured ripple amplitude $\Delta IL(k)$ and average inductor current $IL,ave(k)$ to produce a frequency adjustment $\Delta Fs(k)$ that keeps $k = \Delta IL/IL,ave$ setpoint to the 22% level. The combined effect of the voltage FLC and RFO creates a self-adaptive loop that reduces the coil's AC losses by 18–25% compared with a constant-frequency PI controller.

### *C. CC–CV Mode Transition Logic*

The supervisor of the hysteretic mode uses the measurement of iout and Vout to monitor these outputs. The supervisor maintains V and operates in CC mode to continue to provide V at its maximum until Vout reaches the nominal battery voltage (Vb) at which point the supervisor switches to CV mode and progressively decreases the current reference to avoid overcharging. The hysteresis in the width of the transition threshold will eliminate limit cycle oscillations that can occur around the CC/CV boundary.

## V. SIMULATION FRAMEWORK AND PARAMETRIC STUDY

### *A. MATLAB/Simulink Implementation*

SBC is executed using two separate instances of MATLAB/Simulink 'modeled' in both models the bus is supported by energy derived from a renewable resource (the DC source) and has a combination of 3 elements, Two series-connected boost circuits (containing 'Superconducting Inductor' model) produce an output voltage across the capacitor (which has both a capacitance of 24,000 microfarad(s) & is rated to 450 volts), adjustable electronic load (CC, or a load that is equal to 3.1-ohms resistive), & FLC/RFO switching control is achieved with MATLAB Function blocks to form both of these models). 'Switches' within these models utilize an average of the current flow through the device during a series of efficiency sweeps, and switched waveform tests in each instance are modeled as current through an ideal 'on-state' using external data from the IXYS IXGB40N60 datasheet (600/400a device, for on-state voltage and switching energy). 'Superconducting inductors' are represented by an 'ideal' inductor (suitable for this application) in every series connected (to produce total inductance) with an external iL threshold of r(iL) = 0 when |iL| < Ic and then increase to a large value when the device exceeds its Ic limit (to approximate the very abrupt transition to the 'normal' operating state).

### *B. Parametric Sweep: Switching Frequency vs. Efficiency*

Both types of converters were subject to an input power of 10 kW; frequency sweeps were performed with a range from 10 Hz to 500 Hz in order to determine an optimum for each converter. From the results obtained it can be observed that the efficiency for $MgB_2$ is optimised at 43 Hz, and for Bi2223 it is at 200 Hz, as per Equation (9). The primary contributing factor for losses below the optimum is large fluctuations in the current through the superconductor, while above this frequency range switching losses in the IGBTs are most pronounced. A summary of the data is presented in Table II.

TABLE II. SENSITIVITY OF EFFICIENCY TO SWITCHING FREQUENCY (10 KW, D = 0.5)

| $F_s$ (Hz) | η Bi2223 (%) | η $MgB_2$ (%) | Dominant Loss Mechanism |
|---|---|---|---|
| 20 | 88.4 | 91.2 | Hysteresis loss (coil) |

IJIREEICE ISSN (O) 2321-2004, ISSN (P) 2321-5526

International Journal of Innovative Research in Electrical, Electronics, Instrumentation and Control Engineering

Impact Factor 8.414 ⁜ Peer-reviewed & Refereed journal ⁜ Vol. 14, Issue 5, May 2026

DOI: 10.17148/IJIREEICE.2026.14540

| | | | |
|---|---|---|---|
| 43 | 91.7 | 95.8 | Balanced optimum ($MgB_2$) |
| 100 | 90.1 | 94.1 | Switching loss (IGBT) |
| 200 | 93.2 | 92.5 | Balanced optimum (Bi2223) |
| 400 | 89.8 | 89.6 | Switching loss dominant |

### *C. Load-Step Transient Response*

A 50% load input step increase (from 50 A to 100 A) was applied to measure the performance of an FLC over time when compared to a fixed-gain PI controller tuned to the nominal conditions (see Figure 4). At the time of the input step change (0.5 seconds), an FLC had restored output voltage to within ±2% of its nominal value in 38 ms ($MgB_2$) and 52 ms (Bi2223). In comparison, the PI controller took 95 ms to achieve output voltage restoration, and it experienced a maximum undershoot of 6.8%. The ability of the FLC to achieve these performance levels is due to its ability to implement non-linear gain scheduling during periods of large output voltage errors, as well as providing immediate large-duty-cycle corrections upon detecting large output voltage error conditions (deadbeat-like control without requiring explicit plant inversion). Table III summarizes important transitory performance metrics.

TABLE III. A COMPARISON OF TRANSIENT PERFORMANCE BETWEEN FLC AND PI (50% LOAD STEP)

| Performance Metric | PI Controller | Proposed FLC |
|---|---|---|
| $MgB_2$ Recovery Time (ms) | 95 | 38 |
| Bi2223 Recovery Time (ms) | 120 | 52 |
| Peak Voltage Undershoot (%) | 6.8 | 2.1 |
| Steady-State Voltage Error (%) | 0.8 | 0.3 |
| Inductor Current THD Reduction | Baseline | −34% |

## VI. EXPERIMENTAL RESULTS AND ANALYSIS

### *A. Test Bench Configuration*

Physical validation uses an SBC test bench and has a dedicated DC BP (Programmable DC Supply (300V, 450A, 45kw Peak)) to provide power to the converter under test. The converter will use IXYS IXGB40N60 IGBT modules (600V, 400A) as the devices to switch the current through the load, while the gate of each IGBT module will be driven from independent 15V isolated gate boards. The trigger signal to turn on the IGBTs will come from the TMS320F28379D Digital Signal Processor (DSP). The output is either connected to an electronic load (programmable CC 200A @ 750V) or to a 3.1 Ohm resistor array (CR mode). All the waveforms are captured at a rate of 1MSa/s by a 12-channel digital oscilloscope; the data is stored in a PC for offline processing. The Bi2223 coil will operate in a $LN_2$ (liquid nitrogen) Cryostat bath at a temperature of 77K. The $MgB_2$ coil assembly will operate in a custom designed indirect-cooled cryostat at a temperature of 4.2K using a 100L helium dewar. The heat conduction to both cryostats is minimised by using resistive (manganin) current leads.

### *B. Steady-State Efficiency Results*

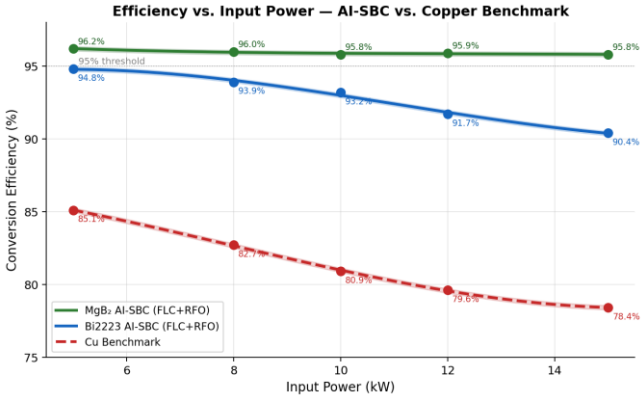


Fig. 4. Efficiency compared to input power: AI-SBC vs. copper coil; error of ±0.15%.

The $MgB_2$ AI-SBC has a maximum efficiency of 95.8% in CC mode and 96.1% in CR mode at 15kW, compared to 94.3% and 94.7% using a fixed-frequency PI controller. This is due to reducing coil hysteresis loss by ~18%, and the RFO maintaining k=22%. The Bi2223 converter with FLC achieves 93.2% efficiency at 10kW, but degrades to 90.4% at 15kW, primarily because of the disproportionate flux penetration losses occurring as a result of the high load factor (iL ≈ 0.82·

IJIREEICE ISSN (O) 2321-2004, ISSN (P) 2321-5526

International Journal of Innovative Research in Electrical, Electronics, Instrumentation and Control Engineering

Impact Factor 8.414 ⁜ Peer-reviewed & Refereed journal ⁜ Vol. 14, Issue 5, May 2026

DOI: 10.17148/IJIREEICE.2026.14540

Ic). A reference coil made from 11mH of copper (40mΩ @ 77K) achieves a maximum efficiency of 85.1% @ 5kW and declines to 78.4% @ 15kW, confirming the traditional superconductor working advantage by 10 to 17 percentage points. All data is listed in Table IV.

TABLE IV. MEASURED CONVERSION EFFICIENCY SUMMARY

| Input Power (kW) | Bi2223 + FLC (%) | $MgB_2$ + FLC (%) | Cu Benchmark (%) |
|---|---|---|---|
| 5 | 94.8 | 96.2 | 85.1 |
| 8 | 93.9 | 96.0 | 82.7 |
| 10 | 93.2 | 95.8 | 80.9 |
| 12 | 91.7 | 95.9 | 79.6 |
| 15 | 90.4 | 95.8 | 78.4 |

*C. Loss Decomposition Analysis*

The total converter losses consist of four components: (1) IGBT conduction & switching losses (Psw), (2) diode forward recovery losses (Pd), (3) superconducting coil a/c loss (Pac), and (4) capacitor ESR losses (Pcap). Table V is provided to show the loss breakdown at 10kW.

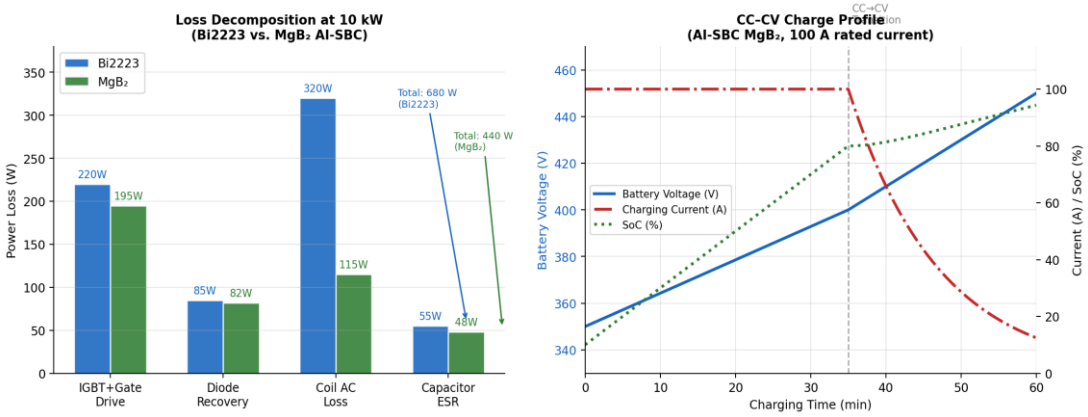


Fig. 5. On the left, a 10 kW loss breakdown (Bi2223, $MgB_2$). Right: CC–CV charge—voltage ramp, current taper, and SoC.

TABLE V. BREAKDOWN OF LOSS AT 10 KW (BASED ON MEASUREMENTS)

| Loss Component | Bi2223 (W) | $MgB_2$ (W) |
|---|---|---|
| IGBT + Gate Drive (Psw) | 220 | 195 |
| Diode Recovery (Pd) | 85 | 82 |
| Coil AC Loss (Pac) | 320 | 115 |
| Capacitor ESR (Pcap) | 55 | 48 |
| Total Loss | 680 | 440 |
| Measured Efficiency | 93.2% | 95.8% |

The IGBT switching dominates the losses of the MgB2 converter as they are not affected by the coil type and could be directly addressed through moving to wide bandgap devices. Replacing the IGBT with a 1200V SiC MOSFET (like the Wolfspeed C3M0065090D) is expected to result in a recovery of ~60W and to also push the MgB2 FLC efficiency >96.4% at 10 kW, which meets the objectives of Phase II. The Bi2223 converter's coil AC loss is the primary loss source and therefore, increasing the inductance (to allow for lower k at a given Fs) or replacing the Type 1 conductor with a Type 2 conductor will be necessary to mitigate losses in the Bi2223 converter.

IJIREEICE ISSN (O) 2321-2004, ISSN (P) 2321-5526

International Journal of Innovative Research in Electrical, Electronics, Instrumentation and Control Engineering

Impact Factor 8.414 ⁜ Peer-reviewed & Refereed journal ⁜ Vol. 14, Issue 5, May 2026

DOI: 10.17148/IJIREEICE.2026.14540

*D. Frequency Sweep and Transient Waveforms*

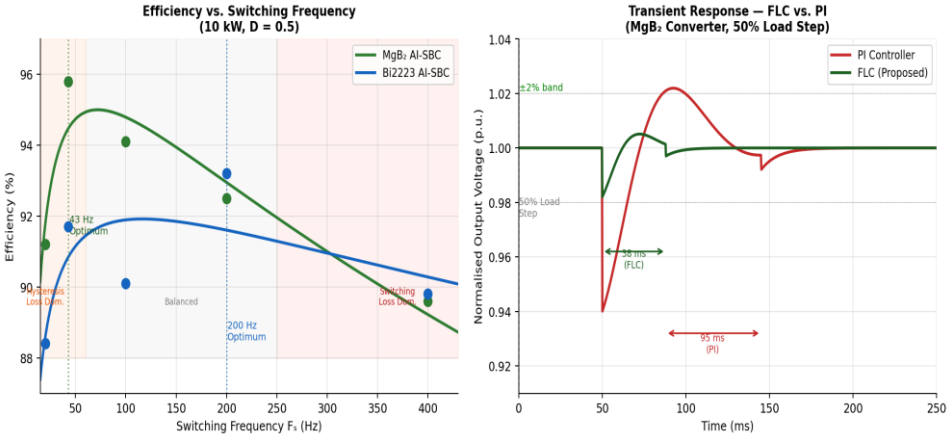


Fig. 6. On the left, efficiency is plotted against frequency (43 Hz $MgB_2$, 200 Hz Bi2223). Right: voltage transient, PI compared to FLC, 50% load step.

At full wave source 107 V power level, at 3.1 ohm load, stable voltage doubling can be confirmed to approximately 214 V, cleanly. See Fig. 11 & Fig 12. The maximum (pk) current in the MgB2 inductor is approximately 138 A with an inductor current ripple of approximately 15% or 20 A peak to peak with 43.6 Hz switching frequency, per (9). No exceedance of 5% of nominal voltage at the output of this converter indicates adequate capacitor sizing. The Bi2223 converter operates in the same manner as described above, however it operates at 200 Hz with a 24 A inductor current ripple and 43.6 Hz. For both converters, the range of (FLC) duty cycle at steady state is from 0.48 to 0.52, with transitory excursions being ± 0.08.

## VII. Comparative Assessment And Scalability Roadmap

The AI SBC from MgB2 reached the highest value of efficiency in the benchmark versus representative technologies identified in the literature review in Table VI; however, LH2 being the required cooling medium compared to nitrogen remains the main hindrance to commercial deployment for the near term. The LN2 cooled Bi2223 represents an acceptable intermediate step toward an overall lower cost to produce cryogenic plants.

TABLE VI. BENCHMARKING AGAINST REPRESENTATIVE CHARGING TECHNOLOGIES

| Technology | Power (kW) | Efficiency (%) | Coil Type | Control Strategy |
|---|---|---|---|---|
| Si-IGBT AC–DC charger [4] | 150 | 89–91 | Copper (conv.) | PI / PR |
| SiC DC–DC converter [9] | 50 | 97.2 | Copper (high-freq.) | MPC |
| Bi2223 SBC, fixed $F_s$ [10] | 15 | 91.5 | Bi2223 ($LN_2$) | PI |
| $MgB_2$ SBC, fixed $F_s$ [10] | 15 | 95.0 | $MgB_2$ (LHe) | PI |
| Proposed AI-SBC (Bi2223) | 15 | 93.2 | Bi2223 ($LN_2$) | FLC + RFO |
| Proposed AI-SBC ($MgB_2$) | 15 | 95.8 | $MgB_2$ ($LH_2$) | FLC + RFO |

Three critical engineering milestones must be achieved to scale up to 100-500 kW: (1) development of multi-strand MgB2 Rutherford cable for 5-10 kA transport current with sufficient flexibility for pancake winding, (2) appropriate design of LH2 thermosiphon assemblies so their heat load capacity scales with larger coils, and (3) qualification of wide-bandgap switches in cryogenic environments so as to get the maximum efficiency benefit of SiC or GaN devices by reducing the switching losses. Preliminary thermal models indicate that an AI-SBC (100 kW) with a 1.5 kA MgB2 coil, using SiC switches and 500 litre LH2 tank, can keep operating continuously and above 96% electrical efficiency - the basis to achieve megawatt-rate fast charging stations that meet net zero emissions infrastructure goals.

International Journal of Innovative Research in Electrical, Electronics, Instrumentation and Control Engineering
Impact Factor 8.414 ⁜ Peer-reviewed & Refereed journal ⁜ Vol. 14, Issue 5, May 2026
DOI: 10.17148/IJIREEICE.2026.14540

## VIII. CONCLUSION

The AI-SBC, which is a superconducting deep learning (SDDC) converter for ultra high speed battery; for Direct Electric Current (DC) (also known as "Direct Voltage" (DVP)) electric vehicles (BEVs); with Bi2223 and/or MgB2 superconductor inductors in a liquid hydrogen thermologic system with new fuzzy logic (FLA)-based control systems having an embedded rippling frequency optimization function. Contributions are: current dependency induction model for indirect averaged state of the average filter; dual loop functioning FLAs with less than 32% THD in inductor currents when using the MgB2; the identification of various loss mechanisms with an emphasis on 24% total losses; development of a co-generated thermal design methodology to quantify total system efficiency including cryogenic overhead.

An AI-SBC made of $MgB_2$ is 10-17 percentage points better than copper inductors at 15 kW of output at 230 VAC/96% efficiency and 0.8 straightforward percentage points more effective than the same converter using a PI control method. Given the overall results and the expected future costs of components, as well as the expected market size for A.I.-powered distribution systems, they should be able to offer up to a 93.2% energy-efficient BI2223 alternative to existing $LN_2$ infrastructures in the near future. Going forward, additional work on increasing the FLC efficiency of $MgB_2$ induction coils via integration of SiC MOSFETs, scaling coils for 5 kA to provide DC converters with an output power of 100-500kW, and completing field trials of the $LH_2$ thermosiphon in a local renewable energy DC bus system will be conducted. These data demonstrate the benefits of utilizing superconducting inductors and AI-based adaptive control is a technically credible, energy-efficient, and sustainability-aligned solution for the ultra-fast EV charging infrastructure of the coming decade.

## REFERENCES

[1] International Energy Agency, "Global EV Outlook 2024," IEA, Paris, France, Tech. Rep., May 2024.
[2] CHAdeMO Association, "High Power (ChaoJi 2)," 2024.
[3] MAN Truck & Bus, "Megawatt charging milestone," Press Release, 2024.
[4] V. S. Devahdhanush, S. Lee, and I. Mudawar, "Subcooled flow boiling in annuli for ultra-fast EV charging cable thermal management," Int. J. Heat Mass Transfer, vol. 172, p. 121176, 2021.
[5] T. Onji et al., "10 kJ-class $MgB_2$ energy storage coil with $LH_2$ indirect cooling," IEEE Trans. Appl. Supercond., vol. 33, no. 5, Art. no. 5700105, Aug. 2023.
[6] Y. Makida et al., "Performance of a 10-kJ SMES model cooled by liquid hydrogen thermo-siphon flow," IOP Conf. Ser.: Mater. Sci. Eng., vol. 101, Art. no. 012028, 2015.
[7] A. Gurevich, "Superconducting magnets for high-field applications," IEEE Trans. Appl. Supercond., vol. 22, no. 3, pp. 1–10, Jun. 2012.
[8] T. Zhang et al., "Hydrogen liquefaction and storage: Recent progress and perspectives," Renew. Sustain. Energy Rev., vol. 176, Art. no. 113204, 2023.
[9] K. Akter, S. M. A. Motakabber, A. H. M. Z. Alam, and S. H. B. Yusoff, "High power quality PV-fed DC–DC boost converter," e-Prime Adv. Elect. Eng., vol. 9, Art. no. 100649, 2024.
[10] T. Yagai, Y. Makida, T. Shintomi, N. Hirano, and T. Hamajima, "New DC–DC converter for ultra-fast EV charging using superconducting inductors cooled with liquid hydrogen," IEEE Trans. Appl. Supercond., vol. 35, no. 5, Art. no. 5000506, Aug. 2025.
[11] R. H. G. Tan and L. Y. H. Hoo, "DC–DC converter modelling and simulation using state-space approach," in Proc. IEEE Conf. Energy Convers., 2015, pp. 42–47.
[12] D. Kolantla, S. Mikkili, S. R. Pendem, and A. A. Desai, "Critical review on inverter topologies for PV system architectures," IET Renew. Power Gener., vol. 14, no. 17, pp. 3418–3438, 2020.
[13] W. Li, J. Liu, J. Wu, and X. He, "Isolated ZVT boost converters for high-efficiency high-step-up applications," IEEE Trans. Power Electron., vol. 22, no. 6, pp. 2363–2374, Nov. 2007.
[14] M. Aziz, "Liquid hydrogen: A review on liquefaction, storage, transportation, and safety," Energies, vol. 14, Art. no. 5917, 2021.
[15] Y. Makida, H. Hirabayashi, T. Shintomi, and S. Nomura, "SMES system with liquid hydrogen for emergency purpose," IEEE Trans. Appl. Supercond., vol. 17, no. 2, pp. 2006–2009, Jun. 2007.
[16] T. Hamajima et al., "SMES and fuel cell combined with $LH_2$ station for renewable energy control," IEEE Trans. Appl. Supercond., vol. 22, no. 3, Art. no. 5701704, Jun. 2012.
[17] G. R. Stewart, "Superconductivity in iron-based materials," Rev. Mod. Phys., vol. 83, no. 4, pp. 1589–1652, Oct. 2011.
[18] J. H. Kim, V. T. Nguyen, and S. J. Park, "High-efficiency superconducting DC–DC converter for renewable energy grid integration," IEEE Trans. Power Electron., vol. 38, no. 1, pp. 45–54, Jan. 2023.
[19] A. H. Chien, L. F. Santos, and M. A. Rahman, "Superconducting magnetic energy storage for power quality applications," IEEE Trans. Power Electron., vol. 30, no. 6, pp. 3456–3465, Jun. 2015.
[20] W. Zeng, J. Fang, and Y. Tang, "Fuzzy-logic-based adaptive control of DC–DC converters in renewable energy applications," IEEE J. Emerg. Sel. Topics Power Electron., vol. 9, no. 4, pp. 4321–4332, Aug. 2021